



Effects of synthesis conditions on the physical and electrochemical properties of $\text{Li}_{1.2}\text{Mn}_{0.54}\text{Ni}_{0.13}\text{Co}_{0.13}\text{O}_2$ prepared by spray pyrolysis

Miklos Lengyel^a, Gal Atlas^a, Dror Elhassid^b, Peter Y. Luo^{a,1}, Xiaofeng Zhang^{a,2}, Ilias Belharouak^{c,3}, Richard L. Axelbaum^{a,*}

^a Department of Energy, Environmental and Chemical Engineering, Washington University in St. Louis, St. Louis, MO 63130, USA

^b X-Tend Energy, LLC, St. Louis, MO 63130, USA

^c Chemical Sciences and Engineering Division, Argonne National Laboratory, 9700 South Cass Avenue, Argonne, IL 60439, USA

HIGHLIGHTS

- Synthesis temperatures between 350 °C–800 °C are evaluated.
- Excellent batch-to-batch reproducibility is obtained.
- At cycle 100 discharge capacities greater than 200 mAh g^{−1} are obtained.
- Primary particle size significantly affects electrochemical performance.

ARTICLE INFO

Article history:

Received 28 November 2013

Received in revised form

4 March 2014

Accepted 24 March 2014

Available online 2 April 2014

Keywords:

Spray pyrolysis

Lithium-ion batteries

Layered lithium–nickel–manganese

–cobalt-oxides

Primary particle size

ABSTRACT

Layered $\text{Li}_{1.2}\text{Mn}_{0.54}\text{Ni}_{0.13}\text{Co}_{0.13}\text{O}_2$ materials were synthesized via spray pyrolysis. Synthesis conditions were varied in order to understand their effect on the electrochemical properties of the material. Three process parameters were evaluated: aerosol flow rate, reactor wall temperature and precursor concentration. Electrochemical results show excellent batch-to-batch reproducibility and no non-uniformities, as measured by energy dispersive X-ray spectroscopy (EDX). Phase purity is maintained for all the samples as measured by powder X-ray diffraction (XRD). The primary particle size has the most significant effect on the electrochemical performance of the materials with smaller primary particles promoting electrochemical activation and increasing capacity. Discharge capacities exceeding 200 mAh g^{−1} after 100 cycles at C/3 rate (where 1C = 200 mAh g^{−1}) are consistently obtained over a wide range of operating conditions. Spray pyrolysis is shown to be a promising, robust synthesis technique for the production of $\text{Li}_{1.2}\text{Mn}_{0.54}\text{Ni}_{0.13}\text{Co}_{0.13}\text{O}_2$ material, delivering excellent electrochemical performance within a wide range of process conditions.

© 2014 Elsevier B.V. All rights reserved.

1. Introduction

Layered composites of Li_2MnO_3 and LiMO_2 (where M = Mn, Ni, Co, etc.) have received significant attention, delivering reversible discharge capacities in excess of 200 mAh g^{−1} [1–4]. To enable commercial implementation of these materials in plug-in hybrid

electric vehicles (PHEVs) and electric vehicles (EVs), a robust synthesis method is required. Conventional synthesis methods include co-precipitation processes, solid-state processes and sol–gel processes [5–7]. Recently, modified versions of these synthesis techniques were successfully developed, such as polymer assisted synthesis routes, solid state combustion synthesis and freeze drying for producing battery materials [8–10]. Most of these processes present significant challenges that can hinder large-scale implementation, such as long reaction times, compositional variations in the product, impurities and batch-to-batch inconsistencies. Solid-state synthesis methods are limited by the solid-state diffusivities and therefore can lead to impurity phases or differences in stoichiometry within the powder, which can compromise the electrochemical performance of the product [11–14]. Sol–gel methods

* Corresponding author. Campus Box 1180, St. Louis, MO 63130, USA. Tel.: +1 314 935 7560; fax: +1 314 935 5464.

E-mail address: axelbaum@wustl.edu (R.L. Axelbaum).

¹ Present address: Princeton University, Princeton, NJ 08544, USA.

² Present address: Argonne National Laboratory, 9700 South Cass Avenue, Argonne, IL 60439, USA.

³ Present address: Qatar Foundation, P.O. Box 5825 Doha, Qatar.

can yield high-quality products, but in general precursors can be expensive and can leave residues in the material [14–16].

Co-precipitation is considered to be the state-of-the-art for the synthesis of layered composite materials and is capable of producing advanced cathode morphologies, such as core–shell type materials with improved stability [17]. Nonetheless, co-precipitation has its technological challenges. Co-precipitation can yield non-uniform composition due to differences in solubility of the various precursors, leading to impurity phases [16,18–22]. While non-uniformities can be reduced via heat treatment, the hold times are long (>10–20 h) and temperatures are high (800–1000 °C) [23,24]. Furthermore, the precipitating agents require several purification steps to be removed and their residues can negatively affect electrochemical performance [20]. These difficulties can also lead to challenges in terms of batch-to-batch reproducibility during large-scale production [16,20].

Spray pyrolysis is a versatile synthesis technique for the production of multi-component metal oxides (e.g.: $\text{YBa}_2\text{Cu}_3\text{O}_7$, $0.3\text{Li}_2\text{MnO}_3 \cdot 0.7\text{LiNi}_{0.5}\text{Mn}_{0.5}\text{O}_2$), including layered lithium-ion battery cathode materials [25–28]. The technical advantages of the process include short residence time (few seconds) in the reactor that allows large throughput; no further post-synthesis purification steps are required; batch-to-batch reproducibility is excellent and the contamination profile of the product meets or exceeds the purity of the precursor [29–32]. Furthermore, spray pyrolysis typically utilizes inexpensive precursor solutions and simple equipment [29]. Finally, the mesoporous morphology of the product allows for complete activation of the material [33–35]. These properties, coupled with excellent electrochemical performance, suggest great potential for commercial implementation.

In spray pyrolysis first a precursor solution is prepared by dissolving appropriate amounts of metal salts, corresponding to the desired stoichiometry [28,29]. The precursor solution is aerosolized to form droplets and particles are subsequently formed in a flow reactor due to the evaporation of the solvent, followed by precipitation and thermal decomposition of the precursor salts [36–38].

The authors have previously reported the synthesis of cobalt-doped materials, and the $\text{Li}_{1.2}\text{Mn}_{0.54}\text{Ni}_{0.13}\text{Co}_{0.13}\text{O}_2$ materials were found to display excellent electrochemical performance [37,38]. Therefore, this chemistry was selected for further optimization. The goal of the present study is to evaluate the effects of synthesis conditions on the electrochemical performance of $\text{Li}_{1.2}\text{Mn}_{0.54}\text{Ni}_{0.13}\text{Co}_{0.13}\text{O}_2$ in order to demonstrate the robustness of the process. Synthesis conditions were varied (including reactor and preheater wall temperature, aerosol flow rate, precursor concentration) and their effects on the electrochemical performance and bulk properties of the material were evaluated.

2. Experimental

Fig. 1 shows a schematic diagram of the modified aerosol flow reactor used for the production of the materials. The precursor solution was prepared by dissolving LiNO_3 , $\text{Mn}(\text{NO}_3)_2 \cdot 4\text{H}_2\text{O}$, $\text{Ni}(\text{NO}_3)_2 \cdot 6\text{H}_2\text{O}$ and $\text{Co}(\text{NO}_3)_2 \cdot 6\text{H}_2\text{O}$ (Alfa Aesar) in deionized water at the ratio corresponding to $\text{Li}_{1.2}\text{Mn}_{0.54}\text{Ni}_{0.13}\text{Co}_{0.13}\text{O}_2$. The total dissolved salt concentration was typically 2.5 mol L^{-1} (M).

The precursor solution was aerosolized using a 2.4 MHz ultrasonic nebulizer (Sonaer Inc.). Water-saturated air was used as the carrier gas at a constant flow rate of 6.6 L per minute (lpm). Residence time in the system was typically 6 s. The aerosol gas stream was carried into a 22 inch long preheater, which was kept at 200 °C, followed by a 3-zone vertical furnace reactor, which had a uniform wall temperature of either 350 °C, 450 °C, 550 °C, 575 °C or 650 °C. One additional high temperature test was conducted where the

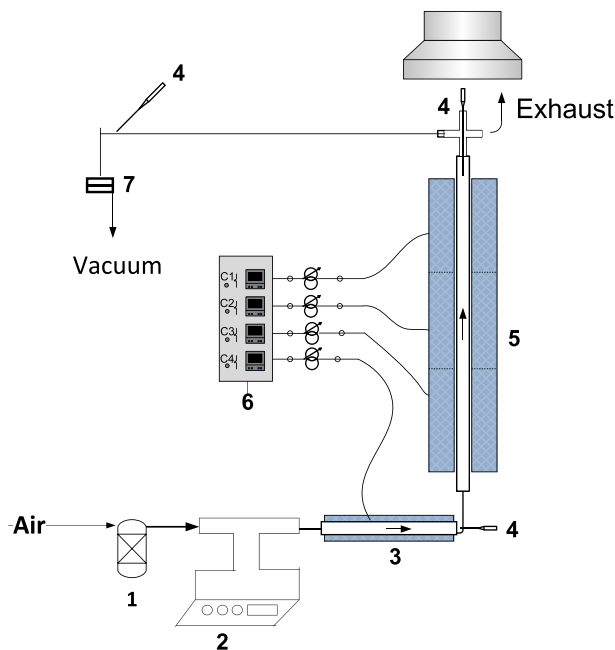


Fig. 1. Schematic diagram of the tubular furnace reactor setup: (1) Bubbler; (2) Ultrasonic nebulizer; (3) 22 inch long preheater; (4) Thermocouple; (5) 3-zone heater; (6) Temperature controller; (7) Porous membrane filter.

preheater was kept at 250 °C and the wall temperature was set to 800 °C. The as-synthesized powders were collected downstream of the reactor on a porous polycarbonate membrane filter (Whatman, GE). The effects of residence time and concentration were studied with fixed preheater wall temperature of 200 °C and reactor wall temperature of 575 °C.

The aerosol particle size distribution was measured using an electrical low-pressure impactor (ELPI Dekati). The as-synthesized powders were subject to annealing heat treatment for 2 h at 900 °C in a box furnace (Thermal Product Solutions). Thermal decomposition of the precursors was analyzed using a thermogravimetric analyzer (TGA Q5000, TA Instruments).

The annealed powders were characterized by XRD using a Rigaku Diffractometer (Geigerflex D-MAX/A) at a scan rate of $0.04^\circ \text{ s}^{-1}$ between 10° and $80^\circ 2\theta$. Structural refinement was performed using the whole pattern fitting (WPF) method in the Jade software. The formula card of $\text{LiNi}_{1/3}\text{Mn}_{1/3}\text{Co}_{1/3}\text{O}_2$ was used as the reference structure for structural refinement. Rietveld-refinement was performed using the EXPGUI software package.

Particle morphology was examined with an FEI Nova 2300 Field Emission scanning electron microscope (SEM). The primary particle size was estimated from SEM images. EDX spectroscopy was used to determine elemental uniformity in the product. Inductively-coupled-plasma mass spectrometry (ICP-MS Perkin Elmer Elan DRC II ICP-MS) was used to determine the composition of the precursor solutions and the annealed powders.

The interior morphology of the product was analyzed by embedding the particles in a Ted Pella epoxy-based resin. Sections 120 nm thick were cut from the dry resin using a Leica Ultramicrotome and the sections were examined by SEM. Tapped powder density was measured using a Quantachrome Autotap tapped density analyzer.

Cathode film fabrication was performed according to the procedure reported earlier [36]. The cathode slurry was prepared using a polyvinylidene fluoride (PVdF) binder solution (Kureha Corp. Japan) and Super-P conductive carbon black (Timcal) suspended in 1-Methyl-2-pyrrolidinone (NMP). Electrochemical performance of

the powders was evaluated in 2032-type coin cells (Hohsen Corporation) assembled in an argon-filled glove box. Half-cells were assembled for electrochemical tests using pure lithium anodes and 2500 Celgard membranes (Celgard, LLC). The electrolyte solution was 1.2 M LiPF₆ in an ethylene carbonate/ethyl-methyl-carbonate solution (EC:EMC = 3:7 by weight) (Tomiya High Purity Chemicals).

Cycling tests and rate capability tests were performed according to the procedures listed in Table 1. Both cycling and rate capability tests were performed using an MTI-BST8-WA battery tester at room temperature, 22 °C.

3. Results and discussion

3.1. Precursor characterization

In a spray pyrolysis process the aerosolized droplets are exposed to significant heating rates. In order to better understand the decomposition reactions occurring in our system TGA analysis was performed on the precursor solution for Li_{1.2}Mn_{0.54}Ni_{0.13}Co_{0.13}O₂ at three different ramp rates: 0.5 °C min⁻¹, 5 °C min⁻¹ and 100 °C min⁻¹. As indicated by the solid line in Fig. 2a, which is for a ramp rate of 0.5 °C min⁻¹ rate, the water (including the crystalline water of the transitional metals) evaporates and then the sample starts to decompose by 70–75 °C. At 5 °C min⁻¹ and 100 °C min⁻¹ the high heating rate does not permit slow evaporation and drying, thus solvent boiling and material decomposition occur almost simultaneously. At 0.5 °C min⁻¹, 5 °C min⁻¹ rate and 100 °C min⁻¹ the thermal decomposition is complete by 400 °C, 475 °C and 525 °C, respectively, indicating a similar behavior to our earlier results [39,40]. Although pure LiNO₃ decomposes around 750 °C, the mixture is completely decomposed by 525 °C at all three ramp rates. As earlier studies have indicated, this result suggests that the decomposition temperature profiles can be affected by the presence of water and transitional metals [41–43]. These studies demonstrated that without further analysis of the individual decomposition events, unambiguous assignment of the peaks in the decomposition profile cannot be made. This is due to the various decomposition reactions involved, as a result of the variable oxidation states of the Ni, Mn and Co ions.

3.2. Reactor temperature effects

Several studies have focused on identifying the effects of reactor temperature on the electrochemical properties of various materials synthesized via spray pyrolysis [44–46]. For a given precursor solution concentration, increasing the synthesis temperature is expected to increase the primary particle size of the materials while

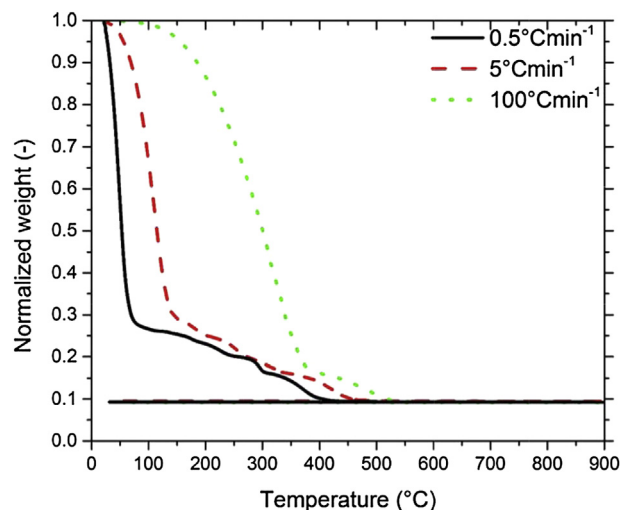


Fig. 2. TGA analysis of decomposition of Li_{1.2}Mn_{0.54}Ni_{0.13}Co_{0.13}O₂ at 0.5 °C min⁻¹, 5 °C min⁻¹ and 100 °C min⁻¹.

having only a minor effect on secondary particle size. Primary particle size can be increased further via post-synthesis annealing, which can lead to longer lithium ion diffusion pathways. Fig. 3 shows the XRD patterns of the as-synthesized powders prepared at reactor temperatures of 350 °C, 575 °C and 800 °C. At a synthesis temperature of 350 °C unreacted lithium nitrate residues were found, as indicated by the arrows in Fig. 3. As expected, these powders were hygroscopic. These results are consistent with results of the TGA study.

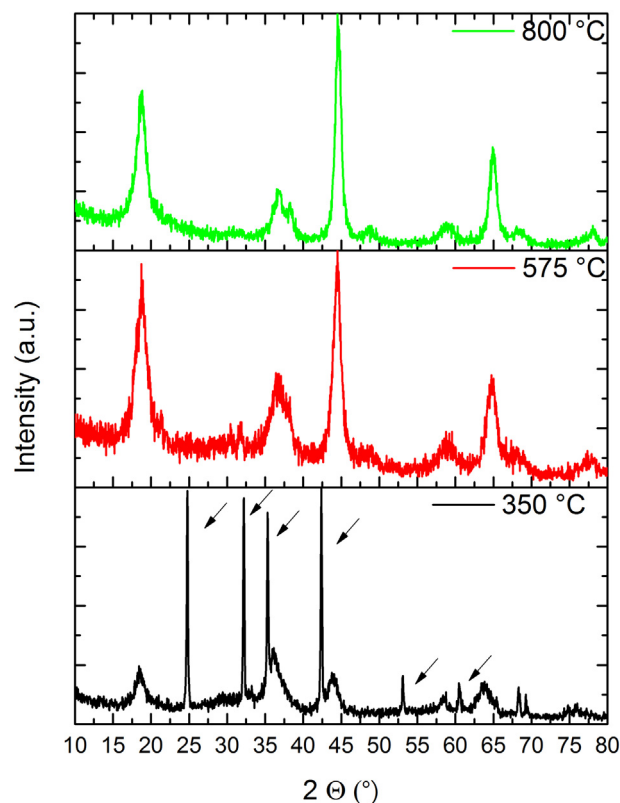


Fig. 3. XRD patterns of the as-synthesized powders synthesized at 350 °C, 575 °C and 800 °C. The arrows indicate the peaks corresponding to LiNO₃ residues in the sample.

Table 1
Testing protocol for rate capability and cycling tests.

	Cycling test protocol (1C = 200 mAh g ⁻¹)	Rate capability test protocol (1C = 200 mAh g ⁻¹)
Activation	1 cycle 2.0–4.8 V at C/10 (20 mA g ⁻¹)	1 cycle 2.0–4.8 V at C/10 (20 mA g ⁻¹)
Subsequent cycles	3 cycles 2.0–4.6 V at C/10 (20 mA g ⁻¹)	4 cycles 2.0–4.6 V at C/10 (20 mA g ⁻¹)
	96 cycles 2.0–4.6 V at C/3 (66.67 mA g ⁻¹)	10 cycles 2.0–4.6 V at C/5 (40 mA g ⁻¹)
		20 cycles 2.0–4.6 V at C/2 (100 mA g ⁻¹)
		40 cycles 2.0–4.6 V at 1C (200 mA g ⁻¹)
		25 cycles 2.0–4.6 V at C/10 (20 mA g ⁻¹)

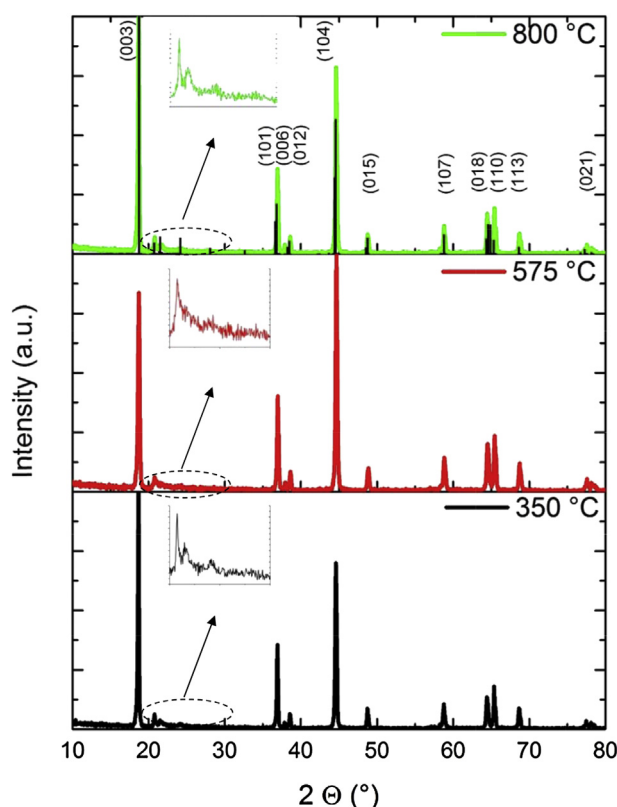


Fig. 4. XRD patterns of the annealed powders synthesized at 350 °C, 575 °C and 800 °C. The insets show the superlattice-reflections occurring between 20 and 25° 2 θ . The standard pdf card is added to the 800 °C pattern using PDF # 04-014-4549.

The as-synthesized particles had a mean particle size of 1.7 μm [37,38]. Increasing the reactor temperature improves the crystallinity of the powder by promoting growth of the primary particles, as indicated by the increase in the intensity of the peaks with

temperature. Similar results for reactor temperature were reported by Kang and Wang for phosphors [44,45]. Based on the XRD patterns of the as-synthesized materials, the following production temperatures were selected for electrochemical testing: 350 °C, 450 °C, 575 °C, 650 °C and 800 °C. All materials were calcined at 900 °C for 2 h before electrochemical testing. The residual LiNO_3 in the as-synthesized samples is not present in the final product. Fig. 4 shows the XRD patterns of powders synthesized at 350 °C, 575 °C and 800 °C after annealing at 900 °C for 2 h. The products are phase pure materials and the spectra are in excellent agreement with those for $\text{Li}_{1.2}\text{Mn}_{0.54}\text{Ni}_{0.13}\text{Co}_{0.13}\text{O}_2$ reported in the literature [1,9,47]. All the materials display the broad-peak between 20 and 25° 2 θ corresponding to the ordering between the Li_2MnO_3 and the LiMO_2 structural components. Rietveld refinement was performed on $\text{Li}_{1.2}\text{Mn}_{0.54}\text{Ni}_{0.13}\text{Co}_{0.13}\text{O}_2$ synthesized at 350 °C, 575 °C and 800 °C. The structures were modeled as a mixture of Li_2MnO_3 and $\text{LiNi}_{1/3}\text{Mn}_{1/3}\text{Co}_{1/3}\text{O}_2$ at a 5:5 ratio [48–50]. Table 2 shows the atomic positions, unit cell parameters and reliability factors, which validate the structural model of the refinement. The different synthesis temperatures cause some variation in the atomic position.

SEM-images were used to evaluate the primary particle size of the annealed powders synthesized at different reactor temperatures (c.f., Fig. 5). After annealing, the primary particles show crystallinity, and the crystal orientation within the secondary particles is random. The particles are nearly equiaxed, allowing the average primary particle size to be estimated according to the procedure of Buesser and Pratsinis [51]. The primary particle size was determined by averaging the results of 100 primary particle measurements and was found to be 335 ± 10 nm, 235 ± 10 nm, 230 ± 10 nm, 320 ± 10 nm and 320 ± 10 nm for powders synthesized at 350 °C, 450 °C, 575 °C, 650 °C and 800 °C, respectively, when annealed at 900 °C for 2 h. At a 350 °C reactor temperature the decomposition is incomplete, as shown in Fig. 3, and this apparently increases the average primary particle size. As discussed below, this may in part be the result of the ill-defined primary particles, caused by the incomplete decomposition.

Table 2

Result of the two phase Rietveld-refinement assuming a phase ratio of 5:5, between Li_2MnO_3 and $\text{LiNi}_{1/3}\text{Mn}_{1/3}\text{Co}_{1/3}\text{O}_2$ for $\text{Li}_{1.2}\text{Mn}_{0.54}\text{Ni}_{0.13}\text{Co}_{0.13}\text{O}_2$ synthesized at 350 °C, 575 °C and 800 °C.

Element	Site	Fractional coordinate			Occup.
Phase I: Li_2MnO_3 (C2/m)					
Li1	2b	0/0/0	0.5/0.5/0.5	0/0/0	0.8540/0.8540/0.8540
Mn1	2b	0/0/0	0.5/0.5/0.5	0/0/0	0.1460/0.1460/0.1460
Li2	2c	0/0/0	0/0/0	0.5/0.5/0.5	1.0/1.0/1.0
Li3	4h	0/0/0	0.6976/0.6810/0.7780	0.5/0.5/0.5	0.9860/0.9860/0.9860
Mn2	4h	0/0/0	0.7283/0.8310/0.6529	0.5/0.5/0.5	0.0140/0.0140/0.0140
Li4	4g	0/0/0	0.1729/0.1687/0.1687	0/0/0	0.0870/0.0870/0.0870
Mn3	4g	0/0/0	0.1705/0.1708/0.1735	0/0/0	0.9130/0.9130/0.9130
O1	4i	0.2988/0.2663/0.1908	0/0/0	0.1939/0.2105/0.2086	1/1/1
O2	8j	0.3040/0.2690/0.1968	0.3252/0.3298/0.3312	0.2236/0.2370/0.2281	1/1/1
a	4.963 Å/4.947 Å/4.940 Å				
b	8.530 Å/8.529 Å/8.521 Å				
c	5.025 Å/5.009 Å/5.021 Å				
β	109.17°/108.94°/109.05°				
Phase II: $\text{LiNi}_{1/3}\text{Mn}_{1/3}\text{Co}_{1/3}\text{O}_3$ ($R\bar{3}m$)					
Li1	3b	0/0/0	0/0/0	0/0/0	0.9700/0.9700/0.9700
Ni1	3b	0/0/0	0/0/0	0/0/0	0.0300/0.0300/0.0300
Li2	3a	0/0/0	0/0/0	0.5/0.5/0.5	0.0300/0.0300/0.0300
Ni2	3a	0/0/0	0/0/0	0.5/0.5/0.5	0.3050/0.3050/0.3050
Mn1	3a	0/0/0	0/0/0	0.5/0.5/0.5	0.3350/0.3350/0.3350
Co1	3a	0/0/0	0/0/0	0.5/0.5/0.5	0.3300/0.3300/0.3300
O1	6c	0/0/0	0/0/0	0.2419/0.2415/0.2407	1.0/1.0/1.0
a	2.851 Å/2.850 Å/2.848 Å				
c	14.233 Å/14.216 Å/14.221 Å				
wR _p	0.2131/0.2152/0.2220		R _p	0.1475/0.1482/0.1557	
Chi ²	1.726/1.833/1.862		Phase ratio	5:5	

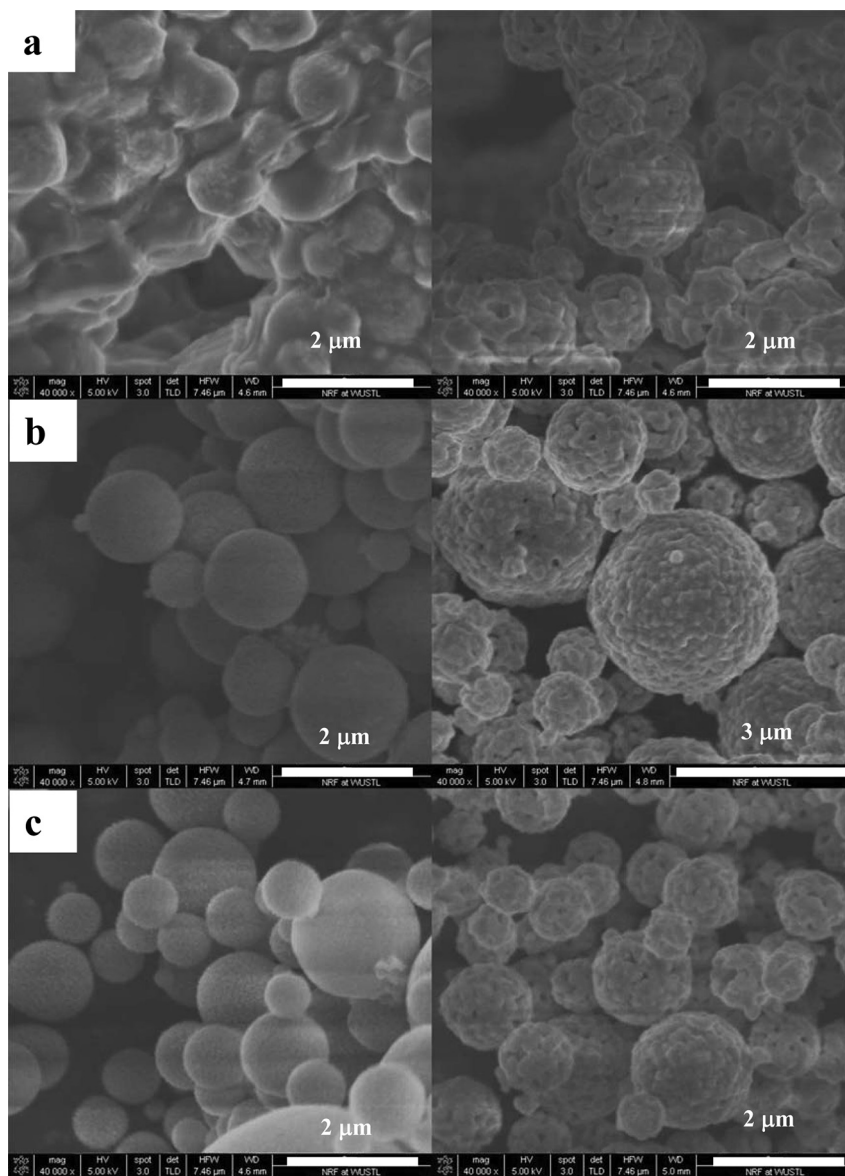


Fig. 5. SEM photographs of powder synthesized at (a) 350 °C; (b) 575 °C; (c) 800 °C. The first column shows the as-synthesized material, and the second column shows the material after annealing at 900 °C for 2 h.

Fig. 5 shows the morphology of the annealed powders produced at 350 °C, 575 °C and 800 °C as observed by SEM. The powder synthesized at 350 °C displays an ill-defined cluster of material (Fig. 5a). Spherical particles are apparent, but the particles display necked structures. The as-produced powder is extremely hygroscopic due to the large amount of LiNO_3 still remaining in the sample. It is speculated that this morphology is a result of partial redissolution of the unreacted nitrates remaining in the sample. After annealing, a spherical shape is more prevalent, but the particles continue to show necks. When the synthesis temperature increases above 575 °C, necking is no longer observed (Fig. 5b). Smaller particles appear to be porous and spherical. Larger particles, typically above 1.5–2 μm , have dents and are irregularly shaped, suggesting that the particles have a hollow interior.

Powders synthesized at 650 °C and 800 °C display similar morphologies to powders synthesized at 575 °C (Fig. 5c). The larger primary particles obtained for the as-synthesized powders at reactor temperatures of 650 °C and 800 °C, as indicated by the XRD

results in Fig. 3, show that reactor temperature is important in defining the ultimate primary particle size [44].

The tap densities of the powders synthesized at various temperatures are listed in Table 3. The largest tap density of 0.86 g cm^{-3} was observed at the temperature where the powder fully decomposes. Below 575 °C, smaller tap densities are likely to be caused by the observed necking, whereas above 575 °C the tap density does not change beyond measurement error. These tap density results are comparable to other lithium-ion battery cathode powders prepared via spray pyrolysis [52]. Further improvements of the tap density are necessary to meet energy density requirements of electric vehicles. Results of recent improvements, where the tap density is increased to $>1 \text{ g cm}^{-3}$, will be discussed in an upcoming paper.

A microtome study was performed on the powder synthesized at 575 °C to characterize the interior morphology, which was observed by SEM (Fig. 6). The particles are composed from 100 to 400 nm size primary particles. When the secondary particles are above 1.8–2.0 μm the particles begin to display a hollow interior.

Table 3

Tap density of the powders synthesized at various reactor temperatures after annealing at 900 °C for 2 h.

Synthesis temperature (°C)	Tapped density (g cm ⁻³)
450	0.60
550	0.64
575	0.86
650	0.78
700	0.77

As discussed by Messing and Jain, hollow sphere formation is a complex phenomenon affected by many parameters [28,53]. Once the precursor solution is aerosolized to form droplets, particles form due to the evaporation of the solvent and the subsequent precipitation of the precursor salts [28]. During the rapid drying period if the surface concentration reaches supersaturation before the core reaches saturation, the likelihood to form hollow spheres increases. Yet, hollow spheres were experimentally observed even for solutions with saturated concentrations throughout the particles [28].

Jain et al. found that hollow sphere formation strongly correlates with the tendency of the precursor salt to melt before the decomposition reaction occurs [53]. For example, they observed that nitrates of Mn, Ni or Co melt before decomposition and that this property correlates with a tendency to form hollow spheres. This can be further complicated if the gases that evolve during decomposition are not able to leave the surface of the particle, i.e. the permeability of the surface during decomposition is low for the evolving gases. This can yield an inflated particle with a hollow interior. Further study is necessary to understand and overcome hollow sphere formation, but this is beyond the goals of the current study.

ICP-MS measurements indicate good agreement between the composition of the materials and the desired chemistry, similar to our earlier report [38]. EDX spectroscopy was performed on the powder synthesized at 575 °C to evaluate the elemental distribution of Mn, Ni, Co and O inside the powder (Fig. 7). The distribution of the elements is uniform throughout the powder. No impurity peaks can be detected by EDX spectroscopy and therefore the XRD pattern of the sample is not displayed.

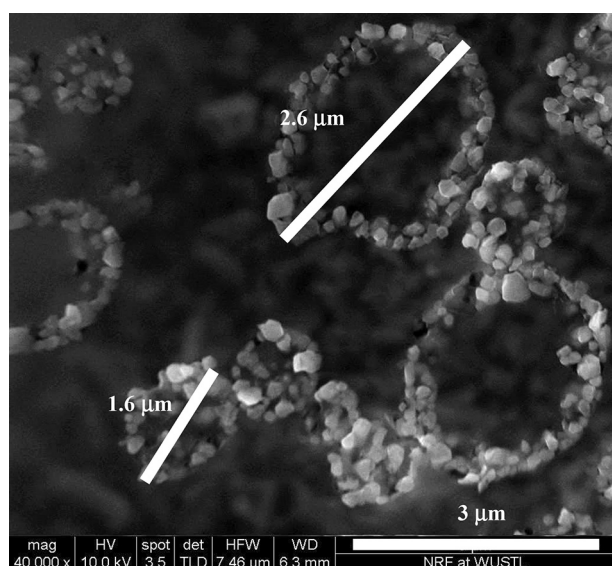


Fig. 6. SEM image showing the interior morphology of the powder.

In summary, the reactor synthesis temperature does not indicate any difference in the XRD-patterns of the powders, and Rietveld-refinement shows minor deviations in the atomic positions. Unreacted LiNO₃, which is present in samples synthesized at 350 °C fully decomposes during the annealing heat treatment. Changes in the synthesis temperature provide us with a method to control primary particle size and the tap density of the powder, but do not present us with a method to reduce the interior hollowness of the structures. Hollow spheres appear to be the main reason behind the low tap density of these materials.

3.3. Precursor concentration effects

Studies indicate that the concentration of the precursor solution correlates with the secondary particle size of the product [53–55]. At a fixed reactor temperature a reduction in concentration reduces the secondary particle size [44]. Several studies demonstrated that by reducing the precursor solution concentration to <<0.5 M the secondary particle size can be controlled accurately for single and simple multi-component oxides, allowing for partial control of hollow sphere formation [28,44,53,56–59]. While these low-concentration studies may help in understanding the fundamental mechanisms of particle formation they do not present a viable option for commercial scale production. Increasing the precursor concentration can also lead to an increase in the number of nucleation sites, which can in turn reduce the primary particle size of the product and improve the electrochemical performance of the material [54,60]. To identify the effect of concentration on the electrochemical performance, three precursor concentrations were studied: 0.5 M, 1 M and 2.5 M. The 0.5 M and 1 M solutions were prepared by diluting the 2.5 M solution to preserve the stoichiometry of the original precursor.

The morphologies of these powders are identical to those in Fig. 5 and therefore are not displayed. The primary particle size of the powder made from the 1 M precursor solution is 240 ± 10 nm, which is very similar to that of the powders synthesized from the 2.5 M precursor. Further dilution of the precursor solution to 0.5 M precursor results in an increase in primary particle size to 350 ± 10 nm. According to Fig. 8 the average secondary particle size of the material synthesized with the 1 M precursor is larger than that for the material synthesized from the 2.5 M precursor. Apparently, the reduced viscosity of the 1 M precursor solution allows larger droplets to form without affecting the nucleation characteristics, as was found in Refs. [44,57,58]. According to these studies the nucleation properties and the droplet size of sprays typically only change when the concentration is decreased below 1 M. The current results display similar trends with the primary particle sizes being 350 ± 10 nm, 240 ± 10 nm and 230 ± 10 nm for the 0.5 M, 1 M and 2.5 M precursor solution, respectively. These results are consistent with homogeneous nucleation theory wherein a more dilute solution will yield less nucleation sites, and the fewer sites will lead to a larger primary particle size [1,44,61].

Changing the concentration of the precursor solution provides us with an additional method to control the primary particle size of the product without impacting phase purity. XRD results indicated no significant difference between the different samples and therefore are not displayed. For the range of concentrations considered here, concentration has a minor effect on secondary particle size. The secondary particle size is essentially determined by the nebulizer used in the synthesis process. Significant reduction in the concentration would be necessary to provide accurate control over the particle size of the product, which would limit the practical application of spray pyrolysis.

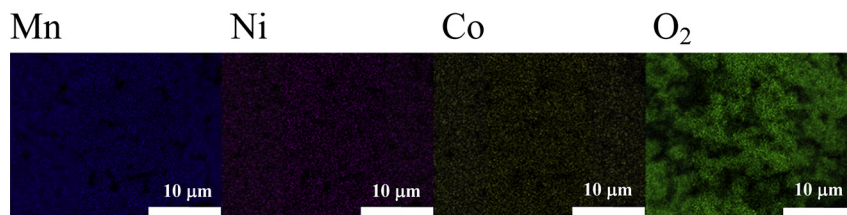


Fig. 7. Elemental distribution of Mn, Ni, Co and O₂ in the powder synthesized at 575 °C at 6.6 lpm flow rate as observed by EDX spectroscopy at 10,000 times magnification.

3.4. Effects of flow rate

The aerosol flow rate and the residence time in the aerosol flow reactor are synonymous parameters in a spray pyrolysis process. Residence time in the reactor will define the time available for decomposition and coarsening at a given reactor temperature, both of which can affect the electrochemical performance of the material. Therefore it is essential to evaluate the effect of residence time on the electrochemical properties at a given reactor temperature. Two flow rates were studied: 6.6 lpm and 10.4 lpm corresponding to 6 s and 4 s residence time.

Fig. 9 shows the particle size distribution of the powders synthesized at these flow rates. The median particle sizes are around 1.5 μm. Increasing the flow rate leads to a drop in the number density, which is speculated to be the result of impaction [29,62].

The morphologies of the as-synthesized and annealed powders prepared at a flow rate of 10.4 lpm are displayed in Fig. 10. The as-synthesized powders form interconnected structures and display similar morphologies to those observed for powders synthesized at 350 °C as displayed in Fig. 5a. The interconnected structures are indicative of unreacted nitrates. The reduction in residence time shows that at this temperature the amount of heat transported into the droplets is insufficient to ensure complete decomposition. It is clear that a certain minimum temperature must be determined and maintained for a given residence time to ensure complete decomposition. Following the annealing heat treatment at 900 °C for 2 h the particles separate into spheres and no obvious necking is observed. The primary particle size due to incomplete decomposition increases to 325 ± 10 nm.

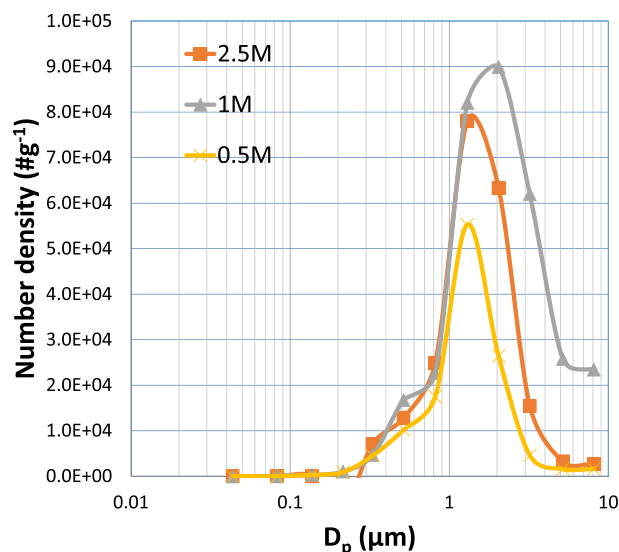


Fig. 8. Particle size distribution of the powder synthesized from 0.5 M, 1 M and 2.5 M precursor solutions.

Figs. 8 and 9 indicate that the secondary particle size is primarily determined by the droplet generation method, with reactor and flow parameters having only a secondary effect. The oscillation frequency of the ultrasonic nebulizer determines the mean droplet size through the Lang equation [28,63]. The resulting particle size (d_p) can be empirically estimated based on the droplet size (d_h). The former is dependent on the densities of the precursor solution and the synthesized oxide, and the latter is dependent on the concentration of the precursor solution, which affects the surface tension and viscosity [63–65]. In order to change the secondary particle size, either a different ultrasonic crystal or a different atomization technique (such as air-assisted atomizers or two-fluid nozzles) must be used [56,66–68].

3.5. Cycling and rate capability tests

To evaluate the effects of synthesis conditions on cycle and rate capability, 8 samples were tested. Half cells were assembled from the materials synthesized at the different temperatures, flow rates and concentrations. The reproducibility of the process was evaluated using charge and discharge tests performed on the material synthesized at 575 °C. The standard deviation for cycling tests was 4 mAh g⁻¹ at C/3 rate during cycle tests based on 4 batches produced under identical conditions on different dates. This indicates excellent batch-to-batch reproducibility.

Fig. 11a–c compare the cycling performance of the materials synthesized at different temperatures, flow rates and concentrations, respectively. Increasing the testing rate from C/10 to C/3 (20 mA g⁻¹ to 66.67 mA g⁻¹) leads to a drop of 35 ± 3 mAh g⁻¹ for the studied chemistries. The average values were obtained by averaging the differences between the respective discharge capacities for the eight materials studied. Among the different synthesis temperatures the powder synthesized at 575 °C displays the

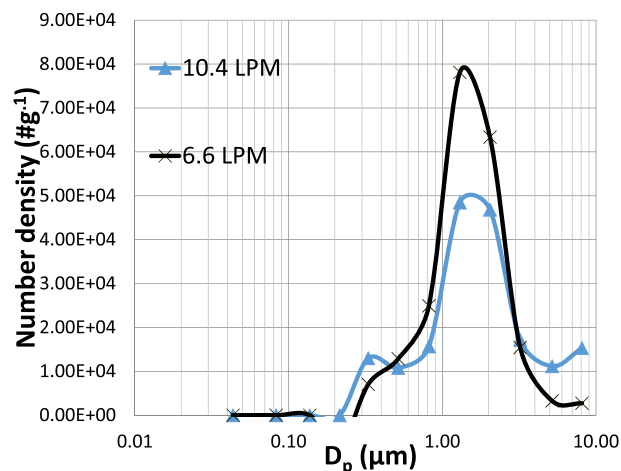


Fig. 9. Particle size distribution of the powder synthesized at 6.6 lpm and 10.4 lpm flow rates.

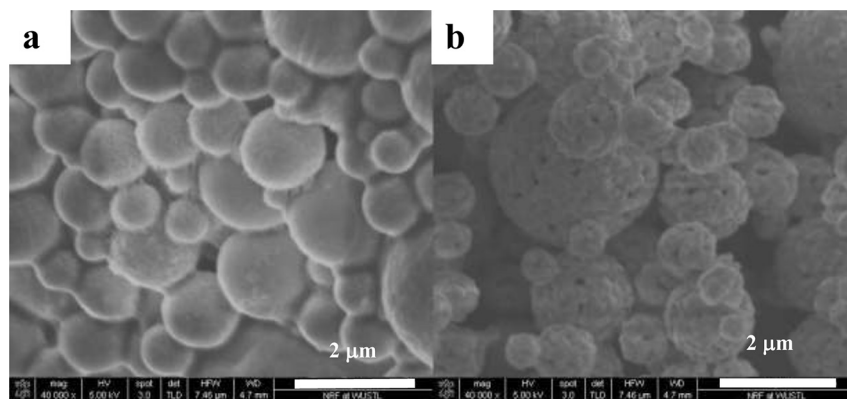


Fig. 10. Morphology of the powder synthesized at 10.4 lpm. (a) As-synthesized; (b) annealed.

highest absolute capacity, showing a 206 mAh g^{-1} discharge capacity after 100 cycles at C/3 rate. The powder synthesized at 800°C displays the lowest capacity: after 100 cycles it retains 162 mAh g^{-1} at C/3 rate. The cycling test results can be correlated to the average primary particle size of the materials (Fig. 12). The smaller primary particle size apparently allows the materials to be

fully activated at 22°C . It is speculated that at a primary particle size of around $320\text{--}340 \text{ nm}$ the core of the primary particles can no longer be fully activated, leading to a reduction in charge and discharge capacity.

The sample synthesized at 350°C has an estimated primary particle size of $335 \pm 10 \text{ nm}$, which is larger than that of the

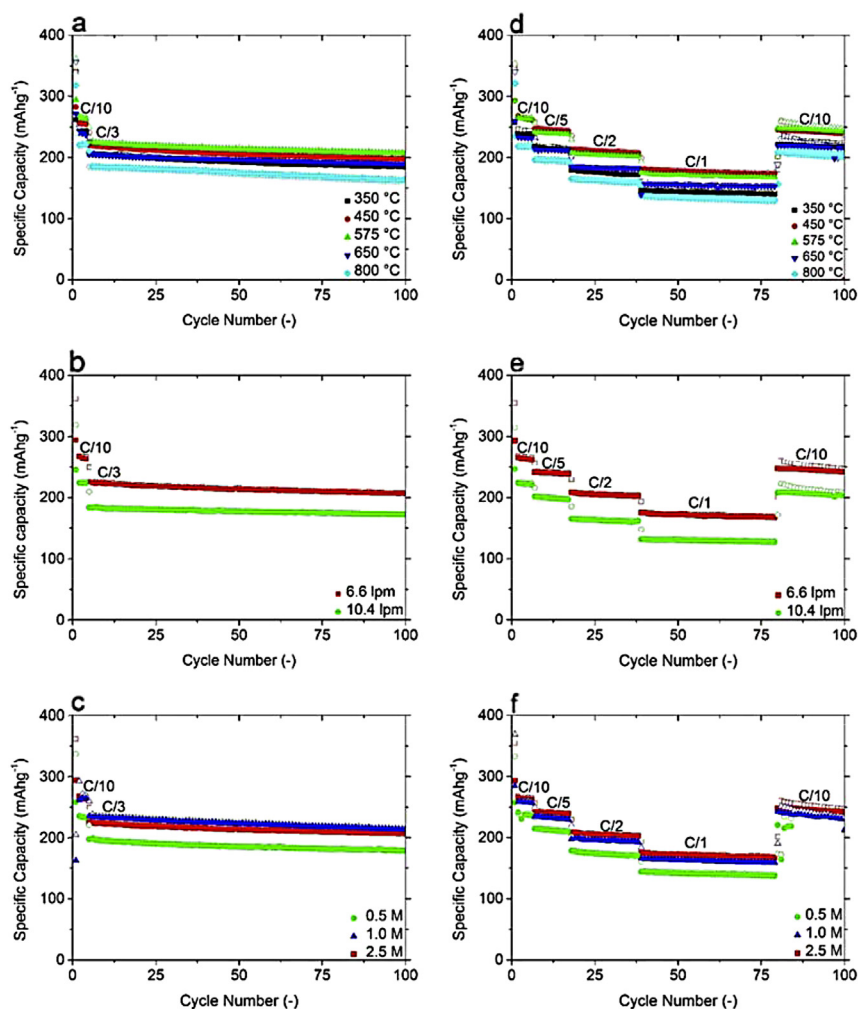


Fig. 11. Cycling performance of cells synthesized at (a) 350°C , 450°C , 575°C , 650°C and 800°C ; (b) 6.6 lpm and 10.4 lpm; (c) 0.5 M, 1 M and 2.5 M precursor solution; Rate capability tests of cells synthesized at (d) 350°C , 450°C , 575°C , 650°C , and 800°C ; (e) 6.6 lpm and 10.4 lpm; (f) 0.5 M, 1 M and 2.5 M precursor solution. The open/solid symbols show charge/discharge capacities, respectively.

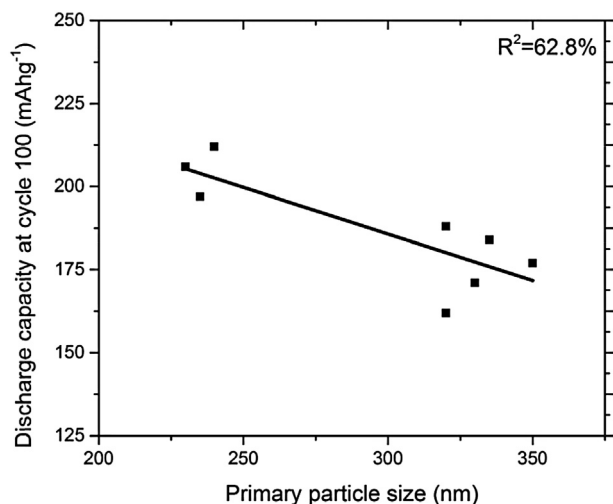


Fig. 12. Particle size vs. discharge capacity after 100 cycles at C/3.

samples synthesized at 800 °C (320 ± 10 nm). Nonetheless, the capacity is slightly higher.

The powder synthesized at a flow rate of 6.6 lpm, displays 206 mAh g^{-1} at cycle 100 at C/3 rate, while the powder synthesized at 10.4 lpm only displays 172 mAh g^{-1} . This is consistent with our observation that the primary particle size of the material synthesized at 10.4 lpm increased to 325 ± 10 nm and that the larger size leads to lower capacity.

The effect of precursor concentration on the cycling performance shows a strong correlation with the primary particle size of the material. The cell prepared from the 0.5 M precursor displays only 177 mAh g^{-1} capacity at cycle 100. The electrochemical performances of the materials prepared from the 1 M and 2.5 M precursor solutions are comparable, as the cells display 206 mAh g^{-1} and 212 mAh g^{-1} capacities, respectively. Thus increasing the precursor concentration enhances the electrochemical performance of the material.

Similar trends can be observed for the rate capability tests of the materials (Fig. 11d–f). For the rate capability tests the increase in testing current from C/10 to C/5, C/2, and C/1 (which corresponds to current densities of 20 mA g^{-1} , 40 mA g^{-1} , 100 mA g^{-1} and 200 mA g^{-1} , respectively) leads to an average drop of 20 ± 3 , 30 ± 3 and $26 \pm 3 \text{ mAh g}^{-1}$ for each step, respectively. The cells fabricated from the materials synthesized at 450 °C and 575 °C display the highest reversible capacity values. At cycle 79, during the last cycle at 1C the materials retain 174 mAh g^{-1} and 169 mAh g^{-1} capacities respectively, which is comparable to materials synthesized via co-precipitation [5,69]. No irreversible

capacity loss is observed. The material synthesized at 10.4 lpm displays lower capacities. While the powder synthesized at 6.6 lpm shows 169 mAh g^{-1} capacity at cycle 79 at 1C rate, the 10.4 lpm powder only displays 128 mAh g^{-1} . The change in the particle size with the precursor concentration has a similar effect, and the powder synthesized from the 1 M and 2.5 M precursor solution retains 160 mAh g^{-1} and 169 mAh g^{-1} , respectively, at cycle 79 at 1C rate, while the powder synthesized from the 0.5 M solution only shows 138 mAh g^{-1} .

According to Fig. 11, for the synthesis temperatures, residence times and precursor concentrations considered, the capacity fade rate or the capacity retention of the material is similar for the conditions studied.

Although some differences can be observed in the morphology of the powder due to differences in the synthesis temperature, no correlation can be identified between the morphology and the electrochemical performance. While studies have revealed that particle shape can be varied with synthesis method [70,71], the spherical morphology is expected to be the most desirable for packing density, provided that hollow spheres can be avoided.

3.6. Voltage fade

Layered materials are known to experience a structural change occurring during cycling that is speculated to be a layered-spinel phase transition [38,47,72–74]. This leads to voltage fade, which has been discussed by recent studies [47,73]. Over cycling, the shapes of the charge and discharge curves change significantly with a shift towards lower voltages, which causes a fade in the battery's energy density.

Fig. 13 compares the dQ/dV curves for cycles 1 and 100 for the materials synthesized at 350 °C, 575 °C and 800 °C. The first cycle curves all display two activation peaks, where the peak above 4.5 V can be associated with the activation of the Li_2MnO_3 component in the structure. The curves at cycle 100 show that reactor temperature has some effect on the voltage fade but the differences are minor, indicating that this structural change cannot be overcome by changes in the synthesis conditions alone.

4. Conclusions

Layered cathode materials were synthesized via spray pyrolysis. The primary and secondary particle sizes of the powders are affected by reactor synthesis temperature, concentration of the precursor and residence time in the reactor. These parameters need to be controlled to achieve optimal electrochemical performance, but the spray pyrolysis process is rather robust in that major changes were not observed and the batch-to-batch reproducibility was excellent. Variations in these parameters provide limited

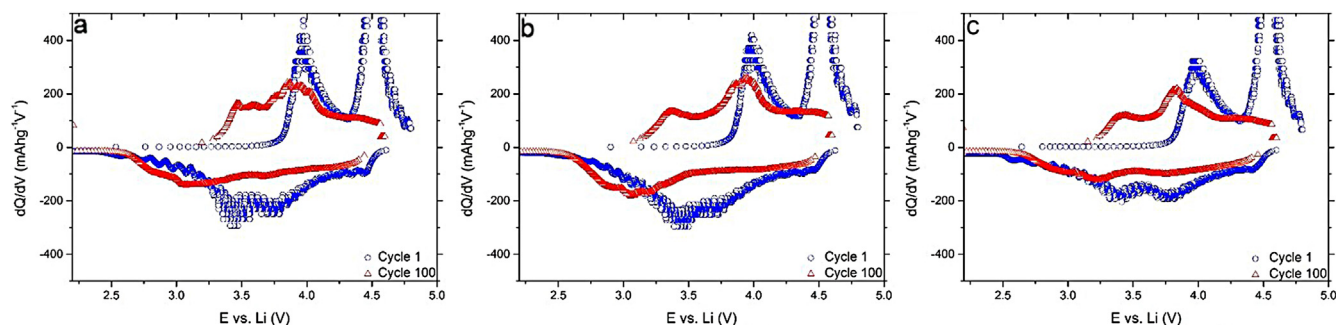


Fig. 13. dQ/dV curves of cycle 1 and cycle 100 of powders synthesized at (a) 350 °C, (b) 575 °C and (c) 800 °C.

control over the morphology of the particles in terms of size, homogeneity and shape.

The three analyzed synthesis parameters (synthesis temperature, concentration and flow rate) allow us to improve the rate capability by changing the primary particle size. Minor differences can be observed in the charge and discharge curves of the materials synthesized at different temperatures. The results clearly show that variations in the synthesis conditions are not capable of preventing the structural change that leads to the voltage fade of these materials.

Compared to other synthesis techniques, our study did not reveal any challenges with batch-to-batch reproducibility, compositional non-uniformities or contaminations in the material. The materials produced in the spray pyrolysis process are phase pure and their contamination meets or exceeds that of the precursor salts. Results indicate that a wide range of process variables exist, wherein spray pyrolysis consistently yields cathode materials with excellent electrochemical performance. Nonetheless, improvements to the tap density are necessary. This study demonstrates that spray pyrolysis is a promising alternative synthesis method for the production of layered cathode materials.

Acknowledgments

The authors are grateful to the NSF and X-tend Energy LLC for their support and to Howard Wynder for the preparation of microtome images and sections. This work was also supported by the Nano Research Facility (NRF – Grant No. ECS-0335765), a member of the National Nanotechnology Infrastructure Network (NNIN), which is supported by the National Science Foundation. Any opinions, findings, conclusions, or recommendations expressed in this material are those of the author(s) and do not necessarily reflect the views of the National Science Foundation. NRF is part of the School of Engineering and Applied Science at Washington University in St. Louis. RLA and Washington University may receive income based on a license of related technology by the University to X-tend Energy, LLC. The results were partly presented at the 2012 Fall meeting of the Materials Research Society, November 2012 in Boston, MA in poster # J 7.03.

References

- [1] C.S. Johnson, N. Li, C. Lefief, M.M. Thackeray, *Electrochem. Commun.* 9 (2007) 787–795.
- [2] M.M. Thackeray, C.S. Johnson, J.T. Vaughey, N. Li, S.A. Hackney, *J. Mater. Chem.* 15 (2005) 2257–2267.
- [3] C.S. Johnson, J.-S. Kim, C. Lefief, N. Li, J.T. Vaughey, M.M. Thackeray, *Electrochem. Commun.* 6 (2004).
- [4] M.M. Thackeray, S.-H. Kang, C.S. Johnson, J.T. Vaughey, R. Benedek, S.A. Hackney, *J. Mater. Chem.* 17 (2007) 3112–3125.
- [5] H. Deng, I. Belharouak, H. Wu, D. Dambournet, K. Amine, *J. Electrochem. Soc.* 157 (2010) A776–A781.
- [6] W.C. West, J. Soler, M.C. Smart, B.V. Ratnakumar, S. Firdosy, V. Ravi, M.S. Anderson, J. Hrbacek, E.S. Lee, A. Manthiram, *J. Electrochem. Soc.* 158 (2011) A883–A889.
- [7] S.-S. Shin, Y.-K. Sun, K. Amine, *J. Power Sources* 112 (2002) 634–638.
- [8] Y. Xu, G. Chen, E. Fu, M. Zhou, M. Dunwell, L. Fei, S. Deng, P. Andersen, Y. Wang, Q. Jia, H. Luo, *RSC Adv.* 3 (2013) 18441.
- [9] F. Amalraj, D. Kovacheva, M. Talianker, L. Zeiri, J. Grinblat, N. Leifer, G. Goobes, B. Markovsky, D. Aurbach, *J. Electrochem. Soc.* 157 (2010) A1121–A1130.
- [10] S.J. Shi, J.P. Tu, Y.Y. Tang, Y.X. Yu, Y.Q. Zhang, X.L. Wang, *J. Power Sources* 221 (2013) 300–307.
- [11] Q. Liu, S. Wang, H. Tan, Z. Yang, J. Zeng, *Energies* 6 (2013) 1718–1730.
- [12] N. Yabuuchi, M. Yano, H. Yoshida, S. Kuze, S. Komaba, *J. Electrochem. Soc.* 160 (2013) A3131–A3137.
- [13] Y. Xiang, Z. Yin, Y. Zhang, X. Li, *Electrochim. Acta* 91 (2013) 214–218.
- [14] A. Mahmoud, J.M. Amarilla, K. Lasri, I. Saadoun, *Electrochim. Acta* 93 (2013) 163–172.
- [15] C. Nythia, R. Thirunakaran, A. Sivashanmugam, G.V.M. Kiruthika, S. Gopukumar, *J. Phys. Chem. C* 113 (2009) 17936–17944.
- [16] J. Shojan, C.V. Rao, L. Torres, G. Singh, R.S. Katiyar, *Mater. Lett.* 104 (2013) 57–60.
- [17] Y.-K. Sun, D.-H. Kim, C.S. Yoon, S.-T. Myung, J. Prakash, K. Amine, *Adv. Funct. Mater.* 20 (2010) 485–491.
- [18] R. Pelosato, C. Cristiani, G. Dotelli, S. Latortora, R. Ruffo, L. Zampori, *J. Power Sources* 195 (2010) 8116–8123.
- [19] D. Wang, I. Belharouak, G. Zhou, K. Amine, *J. Electrochem. Soc.* 160 (2013) A3108–A3112.
- [20] H.-J. Jeon, S.A. Monim, C.-S. Kang, J.-T. Son, *J. Power Sources* 74 (2013) 1185–1195.
- [21] M. Noh, J. Cho, *J. Electrochem. Soc.* 160 (2013) A105–A111.
- [22] D. Liu, J. Han, J.B. Goodenough, *J. Power Sources* 195 (2010) 2918–2923.
- [23] Y. Chen, G. Xu, J. Li, Y. Zhang, Z. Chen, F. Kang, *Electrochim. Acta* 87 (2013) 686–692.
- [24] X. Fang, N. Ding, X.Y. Feng, Y. Lu, C.H. Chen, *Electrochim. Acta* 54 (2009) 7471–7475.
- [25] Y.J. Hong, J.H. Kim, M.H. Kim, Y.C. Kang, *Mater. Res. Bull.* 47 (2012) 2022–2026.
- [26] S.H. Park, C.S. Yoon, S.G. Kang, H.-S. Kim, S.-I. Moon, Y.-K. Sun, *Electrochim. Acta* 49 (2004) 557–563.
- [27] L.J. Fu, H. Liu, C. Li, Y.P. Wu, E. Rahm, R. Holze, H.Q. Wu, *Prog. Mater. Sci.* 50 (2005).
- [28] G.L. Messing, S.C. Zhang, G.V. Jayanthi, *J. Am. Ceram. Soc.* 76 (1993) 2707–2726.
- [29] T.T. Kostas, M.J. Hampden-Smith, *Aerosol Processing of Materials*, Wiley-VCH Publication, 1999.
- [30] M.T. Htay, Y. Hashimoto, N. Momose, K. Ito, *J. Cryst. Growth* 311 (2009) 4499–4504.
- [31] B. Schimmoller, F. Hoxha, T. Mallat, F. Krumeich, S.E. Pratsinis, A. Baiker, *Appl. Catal. A* 374 (2010) 48–57.
- [32] K. Konstantinov, S.H. Ng, J.Z. Wang, G.X. Wang, D. Wexler, H.K. Liu, *J. Power Sources* 159 (2006) 241–244.
- [33] P.G. Bruce, B. Scrosati, J.-M. Tarascon, *Angew. Chem. Int. Ed.* 47 (2008) 2930–2946.
- [34] Q. Qu, L. Fu, X. Zhan, D. Samuelis, J. Maier, L. Li, S. Tian, Z. Li, Y. Wu, *Energy Environ. Sci.* 4 (2011) 3985–3990.
- [35] P. Balaya, K. Saravanan, V. Ramar, H.S. Lee, M. Kueza, S. Devaraj, D.H. Nagaraju, K. Ananthanarayanan, C.W. Mason, in: *Proc. SPIE, Orlando, Florida*, 2011.
- [36] X. Zhang, R.L. Axelbaum, *J. Electrochem. Soc.* 159 (2012) A834–A842.
- [37] X. Zhang, M. Lengyel, I. Belharouak, R.L. Axelbaum, in: *221st Meeting of the Electrochemical Society, Seattle*, 2012.
- [38] M. Lengyel, X. Zhang, G. Atlas, H.L. Bretscher, I. Belharouak, R.L. Axelbaum, *J. Electrochem. Soc.* (2014) under review.
- [39] X. Zhang, H. Zheng, V. Battaglia, R.L. Axelbaum, *J. Power Sources* 196 (2011) 3640–3645.
- [40] X. Zhang, PhD Thesis, Washington University in St. Louis, 2011.
- [41] K.H. Stern, *High Temperature Properties and Thermal Decomposition of Inorganic Salts with Oxyanions*, CRC Press, 2000.
- [42] W. Brockner, C. Ehrhardt, M. Gjika, *Thermochim. Acta* 456 (2007) 64–68.
- [43] T. Nissinen, M. Leskelä, M. Gasik, J. Lamminen, *Thermochim. Acta* 427 (2005) 155–161.
- [44] W.-W. Wang, W. Widiyastuti, T. Ogi, I.W. Lenggoro, K. Okuyama, *Chem. Mater.* 19 (2007) 1723–1730.
- [45] Y.C. Kang, S.B. Park, I.W. Lenggoro, K. Okuyama, *J. Mater. Res.* 14 (1999) 2611.
- [46] T. Minami, W.-N. Wang, F. Iskandar, K. Okuyama, *Jpn. J. Appl. Phys.* 47 (2008) 7220–7223.
- [47] Y. Li, M. Bettge, B. Polzin, Y. Zhu, M. Balasubramanian, D.P. Abraham, *J. Electrochem. Soc.* 160 (2013) A3006–A3019.
- [48] S.-C. Yin, Y.-H. Rho, I. Swainson, L.F. Nazar, *Chem. Mater.* 18 (2006) 1901–1910.
- [49] J. Choi, A. Manthiram, *J. Mater. Chem.* 16 (2006) 1726–1733.
- [50] A. Boulineau, L. Croguennec, C. Delmas, F. Weill, *Chem. Mater.* 21 (2009) 4216–4222.
- [51] B. Buesser, S.E. Pratsinis, *Annu. Rev. Chem. Biomol. Eng.* 3 (2012) 103–127.
- [52] I. Taniguchi, N. Fukuda, M. Konarova, *Powder Technol.* 181 (2008) 228–236.
- [53] S. Jain, D.J. Skamser, T.T. Kostas, *Aerosol Sci. Technol.* 27 (1997) 575–590.
- [54] K.H. Leong, *J. Aerosol Sci.* 18 (1987) 525–552.
- [55] K.Y. Jung, J.H. Lee, H.Y. Koo, Y.C. Kang, S.B. Park, *Mater. Sci. Eng. B* 137 (2007) 10–19.
- [56] S.-C. Zhang, G.L. Messing, *J. Am. Ceram. Soc.* 73 (1990) 61–67.
- [57] S.-C. Zhang, G.L. Messing, W. Huebner, *J. Aerosol Sci.* 22 (1991) 585–599.
- [58] A. Gurav, T. Kostas, T. Pluym, Y. Xiong, *Aerosol Sci. Technol.* 19 (1993).
- [59] Y. Xiong, T.T. Kostas, *J. Aerosol Sci.* 24 (1993) 893–908.
- [60] K.H. Leong, *J. Aerosol Sci.* 18 (1987) 511–524.
- [61] G.F. Arkenbout, *Melt Crystallization Technology*, first ed., Technomic, Basel, 1995.
- [62] C. Cramer, P. Fischer, E.J. Windhab, *Chem. Eng. Sci.* 59 (2004) 3045–3058.
- [63] R.J. Lang, *J. Acoust. Soc. Am.* 34 (1962) 6.
- [64] T. Mokkelbost, I. Kaus, R. Haugsrud, T. Norby, T. Grande, M.-A. Einarsrud, *J. Am. Ceram. Soc.* 91 (2008) 879–886.
- [65] B.W. Mwakikunga, *Crit. Rev. Solid State Mater. Sci.* 39 (2014) 46–80.
- [66] X. Zhang, M. Lengyel, R.L. Axelbaum, *AIChE J.* 60 (2014) 443–450.

- [67] P. Thybo, L. Hovgaard, J.S. Lindeløv, A. Brask, S.K. Andersen, *Pharm. Res.* 25 (2008) 1610.
- [68] N. Kieda, G.L. Messing, *J. Mater. Res.* 13 (1998) 1660.
- [69] S.-H. Kang, M.M. Thackeray, *Electrochem. Commun.* 11 (2009) 748–751.
- [70] X. Luo, X. Wang, L. Liao, S. Gamboa, P.J. Sebastian, *J. Power Sources* 158 (2006) 654–658.
- [71] A. Cao, A. Manthiram, *Phys. Chem. Chem. Phys.* 14 (2012) 6724–6728.
- [72] X. Yu, K. Nam, E. Hu, D.P. Abraham, X. Yang, in: 222nd Meeting of the Electrochemical Society, Oahu, Hawaii, 2012.
- [73] D. Mohanty, S. Kalnaus, R.A. Meisner, K.J. Rhodes, J. Li, E.A. Payzant, D.L. W III, C. Daniel, *J. Power Sources* 229 (2013) 239–248.
- [74] B. Song, Z. Liu, M.O. Lai, L. Lu, *Phys. Chem. Chem. Phys.* 14 (2012) 12875–12883.